Applied Acoustics 213 (2023) 109655

Contents lists available at ScienceDirect

Applied Acoustics

journal homepage: www.elsevier.com/locate/apacoust

Broadband low-frequency sound insulation of a metamaterial plate with inertial amplification

Chenyang Xi [a], Xiang Yu [b], Li Cheng [b], Yongzhen Mi [a,*]

[a] Institute of High Performance Computing (IHPC), Agency for Science, Technology and Research, (A*STAR), 1 Fusionopolis Way, #16-16 Connexis, Singapore 138632, Singapore
[b] Department of Mechanical Engineering, The Hong Kong Polytechnic University, 999077 Hong Kong, China

ARTICLE INFO

Keywords:
Inertial amplification
Acoustic metamaterial
Early coincidence
Sound insulation

ABSTRACT

The recent development of Inertia Amplification (IA) acoustic metamaterial (AMM) opens a new venue for insulating low-frequency sound waves. This differs from conventional approaches that rely excessively on the structural density of the insulator and, therefore, lead to prohibitively heavy structures. The IA-AMM acquires a large effective density and a broad flexural bandgap by amplifying the inertia of many small mass elements periodically distributed in its unit cells, thus holding great promise as an effective yet lightweight solution for low-frequency sound insulation. This paper explores this possibility through numerical and experimental investigations. A semi-analytical model of an IA-AMM plate is developed by combining analytical equations characterizing the kinematics of an IA mechanism and FEM equations governing the vibration of the host plate. Based on this model, sound transmission characteristics of the plate under various sound incidences are analyzed with different amplification angles. By comparing with a locally resonant AMM plate, we found that the IA-AMM plate's sound transmission losses (STLs) are significantly and systematically improved over a wide frequency range of 116–544 Hz. To understand the underlying physics, the band diagram of the IA-AMM plate is calculated, which indicates the formation of a flexural bandgap covering the frequencies of the improved STL. The velocity contour of the plate at the center frequency of this bandgap also reveals much-suppressed vibration velocity amplitudes and a dipole-like sound radiation directivity, further explaining the observed enhancement of the sound insulation ability. Numerically predicted improvement of sound insulation is finally confirmed by experiments.

1. Introduction

Insulating sounds at low frequencies is technically challenging and practically important. At high frequencies, where acoustic wavelengths are short, acoustic waves can be efficiently attenuated by an insulator designed with small-sized soundproof treatments that interact strongly with the incident sound at a scale close to the wavelength [1]. Traditional sound insulators, such as microperforated plates [2,3] and porous foams [4,5], can be lightweight and compact while performing reasonably well. However, as the frequency moves downwards, acoustic wavelengths become more prolonged, and the insulator-sound interaction becomes less intensive, gradually decreasing sound insulation performance. As a promising solution, acoustic metamaterials (AMMs) have drawn increasing attention in recent years [6]. AMMs are built by periodically arranging a cluster of functional modules called unit cells. The collective resonant behavior of the unit cells endows AMMs with the unique property of *bandgap* – a continuous frequency range in which flexural waves, a dominant source of sound radiation, are prohibited from propagation [7,8]. Therefore, the bandgap property, whose cut-on frequency is favorably adjustable, offers a new dimension to tackle the low-frequency sound insulation problem [9–11].

The application of locally resonant (LR) AMMs for sound insulation has been widely studied, with extensive results found in the literature. Such efforts start from [12], which confirms the feasibility of using arrays of spring-mass resonators to enhance the sound insulation ability of a homogenous thin plate. This work also reported an intriguing phenomenon – *early coincidence* – during sound transmission through an LR-AMM plate. Like the classical coincidence between acoustic and bending waves [13], early coincidence causes a sudden and substantial fall on the STL curve. Alternatively, shunted piezoelectric patches can realize the

* Corresponding author.
E-mail address: mi_yongzhen@ihpc.a-star.edu.sg (Y. Mi).

https://doi.org/10.1016/j.apacoust.2023.109655
Received 29 May 2023; Received in revised form 14 September 2023; Accepted 15 September 2023
Available online 18 September 2023

local resonators instead of mechanical spring-mass units [14]. Either way, it is found that the local resonance bandgap is effective only over a narrow frequency range. Improvements to this limitation include damping treatment [15], graded arrangement of resonators [16], or replacing every single resonator with a set of resonators tuned to resonate at successive frequencies [17]. To combine the advantages of acoustic metamaterials and traditional composite panels, the STL of metamaterial double panels is investigated in [18], focusing on suppressing the valley caused by the mass-air-mass resonance. In [19], the same idea is extended to a sandwich panel with a honeycomb core, where vibration and sound radiation reductions are numerically studied and experimentally verified.

Despite those proven advantages, the research of AMM still faces significant obstacles. The resonance frequency of the attached unit cell determines the cut-on frequency of the local resonance bandgap. Therefore, moving the bandgap to low frequencies inherently requires the unit cell to grow in weight (when spring-mass units act as local resonators) or in size (when Helmholtz resonators are used instead). Ultimately, it leads to excessively bulky or prohibitively heavy sound insulators that are not feasible for practical use. To address this problem, inertial amplification (IA) AMMs have recently attracted significant attention as an alternative to local resonance AMMs [20–22]. Besides the use of periodic IA mechanisms to create a bandgap far wider than its locally resonant counterpart, the most salient feature is the possibility of lowering the bandgap frequency by adding virtual inertia to the unit cells – achieved by simply turning up the amplification angle of the mechanism [23,24].

Compared with the LR-AMM, the inertial amplification AMM is less studied to date, but it has demonstrated the potential to cope with challenging vibration and noise reduction tasks. A network of studies on the design, analysis, and optimization of the IA-AMM lattice has been conducted by Yilmaz and co-workers in the past decade [25–27], showing its superiorities in bandgap generation, wave propagation manipulation, and lightweight structure design. The incorporation of IA mechanisms into continuous structures has been investigated by Frandsen et al. [28] for longitudinal wave control in elastic rods and Li et al. [29] for transverse vibration isolation in phononic beams. Recently, IA has been utilized to induce wide and low-frequency bandgaps in corrugated sandwich plates [30]. Synergies between local resonance and inertial amplification are also sought by Banerjee et al. [31] in their studies to couple a levered mass with an LR mass.

Our primary motivation in this work is to explore whether the advantages of the IA-AMMs could be leveraged to enhance the low-frequency sound insulation ability of a thin plate, which, limited by the mass law [32], is still heavy and bulky. As proof of concept, this idea was investigated using an inertially amplified AMM beam in our previous work [33]. Despite the ease of theoretical deviation, beam structures are unrealistic for real-life soundproofing. Therefore, whether those appealing properties could be sustained on a plate must be answered. Since a beam and a plate are fundamentally different, with the latter bearing much richer dynamics and a more complicated wave phenomenon, the extra dimension of a plate can be exploited to achieve further sound attenuation by redistributing vibration energy over the two-dimensional plane. Driven by such an energy redistribution, a beneficial cancellation of radiated sound is expected. In this work, a semi-analytical model for the IA-AMM plate is developed in Section 2, which is used to investigate the sound insulation properties of the IA-AMM plate in Section 3. The numerically predicted sound insulation improvement will be verified through experiments in Section 4.

2. Theoretical model and formulation

Fig. 1(a) illustrates the proposed IA-AMM plate impinged by an incident plane wave with sound pressure p_i, generating reflected and transmitted waves p_r and p_t, respectively. The direction of the incident sound is denoted by azimuth θ and elevation φ angles. The plate has Young's modulus E, Poisson's ratio ϑ, mass density ρ_s, thickness h, and is assumed to be simply-supported along the boundaries. A unit cell of the IA-AMM plate consists of the substrate panel and the inertia amplification mechanism, as shown in Fig. 1(b). The main component of the mechanism is a linkage of four rigid bars forming a pyramid shape, which bridges the substrate panel and a small mass via eight moment-free pivots on both ends of each bar. These bars are made of high-stiffness and low-density material, so their masses and deformation will not be considered in the following formulation.

The transverse vibration of the plate, induced by the incident plane wave, drives the small mass to move horizontally and vertically. The initial and deformed configurations of the mechanism are shown in Fig. 1(c). Specifically, the vertical distance between the lumped mass and the mid-surface of the host plate is defined as H. The relations between the displacements of the mass, denoted respectively by q_1, q_2, and q_3 in the x-, y-, and z-directions, and the transverse displacements of the

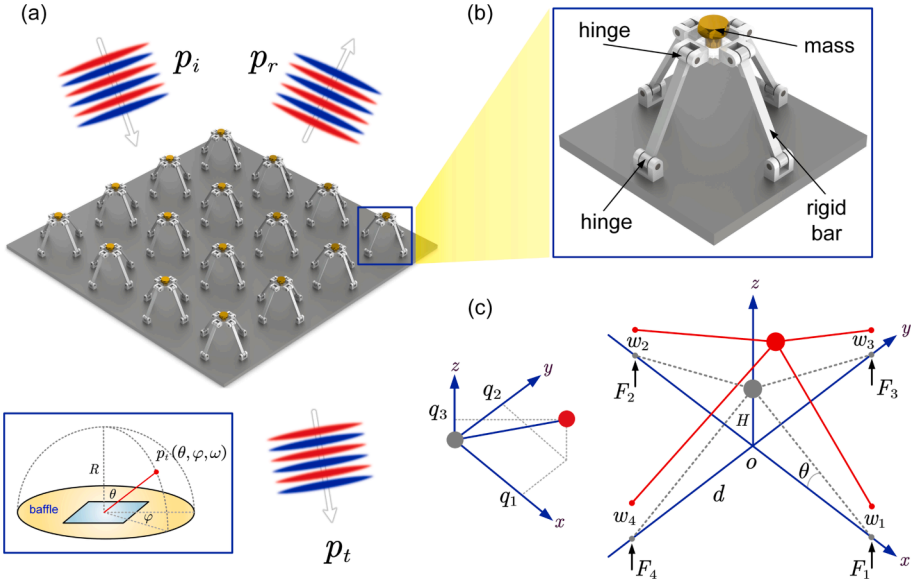

Fig. 1. Schematic of the IA-AMM plate: (a) plane wave transmission through an IA-AMM plate; (b) close view of one single unit cell taken from the IA-AMM plate; (c) initial and deformed configurations of the IA mechanism.

plate, denoted respectively by w_1, w_2, w_3, and w_4 at the four hinge connections, are expressed as [29]:

$$\begin{cases} (q_1+d)^2+q_2^2+(q_3+H-w_1)^2=l^2 \\ (q_1-d)^2+q_2^2+(q_3+H-w_2)^2=l^2 \\ q_1^2+(q_2+d)^2+(q_3+H-w_3)^2=l^2 \\ q_1^2+(q_2-d)^2+(q_3+H-w_4)^2=l^2 \end{cases} \tag{1}$$

in which l is the length of the rigid bars.

Equation. (1) could be linearized based on the assumption that the mechanism undergoes minor deformation so that w_1, w_2, w_3, and w_4 are much smaller than H. The following relations are steadily obtained after the linearization:

$$\begin{cases} q_1=\dfrac{H}{2d}(w_1-w_2)=\dfrac{\tan\alpha}{2}(w_1-w_2) \\ q_2=\dfrac{H}{2d}(w_3-w_4)=\dfrac{\tan\alpha}{2}(w_3-w_4) \\ q_3=\dfrac{w_1+w_2+w_3+w_4}{4} \end{cases} \tag{2}$$

The kinematics of the inertial amplification mechanism is derived based on Lagrange's equation, written as

$$\frac{d}{dt}\left(\frac{\partial L}{\partial \dot{q}}\right)-\frac{\partial L}{\partial q}=0 \tag{3}$$

The Lagrangian L in Eq. (3) is calculated as $L=T-V+W$ where T, V, and W are kinematic energy, potential energy, and work done by the external forces, respectively. The detailed expressions of the three terms are:

$$\begin{cases} T=\dfrac{1}{2}m_a\left(\dot{q}_1^2+\dot{q}_2^2+\dot{q}_3^2\right) \\ V=0 \\ W=F_1w_1+F_2w_2+F_3w_3++F_4w_4 \end{cases} \tag{4}$$

Substituting Eq. (2) into Eq. (4) and further into Eq. (3), we obtain a new set of equations written in terms of w_1, w_2, w_3, and w_4:

$$\begin{cases} \dfrac{m_a}{4}\tan^2\alpha\left(\ddot{w}_1-\ddot{w}_2\right)+\dfrac{m_a}{16}\left(\ddot{w}_1+\ddot{w}_2+\ddot{w}_3+\ddot{w}_4\right)-F_1=0 \\ \dfrac{m_a}{4}\tan^2\alpha\left(\ddot{w}_2-\ddot{w}_1\right)+\dfrac{m_a}{16}\left(\ddot{w}_1+\ddot{w}_2+\ddot{w}_3+\ddot{w}_4\right)-F_2=0 \\ \dfrac{m_a}{4}\tan^2\alpha\left(\ddot{w}_3-\ddot{w}_4\right)+\dfrac{m_a}{16}\left(\ddot{w}_1+\ddot{w}_2+\ddot{w}_3+\ddot{w}_4\right)-F_3=0 \\ \dfrac{m_a}{4}\tan^2\alpha\left(\ddot{w}_4-\ddot{w}_3\right)+\dfrac{m_a}{16}\left(\ddot{w}_1+\ddot{w}_2+\ddot{w}_3+\ddot{w}_4\right)-F_4=0 \end{cases} \tag{5}$$

Assuming a harmonic dependency on time t ($w_i=W_ie^{-j\omega t}$, where ω is the angular frequency and j is the imaginary unit), Eq. (5) is organized to the matrix form:

$$-\omega^2\mathbf{M}^a\mathbf{W}^a=\mathbf{F}^a \tag{6}$$

in which $(\mathbf{W}^a)^{\mathrm{T}}=[W_1\ W_2\ W_3\ W_4]$ is the displacement vector of the mechanism; $(\mathbf{F}^a)^{\mathrm{T}}=[F_1\ F_2\ F_3\ F_4]$ is the load vector of the mechanism; $\mathbf{M}^a$ is the mass matrix of the mechanism, written as

$$\mathbf{M}^a=\frac{m_a}{16}\begin{bmatrix} 4\tan^2\alpha+1 & 1-4\tan^2\alpha & 1 & 1 \\ 1-4\tan^2\alpha & 4\tan^2\alpha+1 & 1 & 1 \\ 1 & 1 & 4\tan^2\alpha+1 & 1-4\tan^2\alpha \\ 1 & 1 & 1-4\tan^2\alpha & 4\tan^2\alpha+1 \end{bmatrix} \tag{7}$$

Equation. (7) clearly shows the role of the amplification angle α through its diagonal submatrices and coupling of the x- and y-direction motions through its off-diagonal submatrices.

Since Eq. (6) is expressed in terms of the plate displacement, it is straightforward to couple it with the finite element equation of the plate vibration by assembling the same degrees of freedom. By coupling Eq. (6) with the FEM equation of the host plate, the force term on the right-hand side of Eq. (6) will be balanced by its counterpart from the plate side and therefore naturally vanishes. The semi-analytical equation after the assembly is written as

$$\left[\mathbf{K}^p-\omega^2\left(\mathbf{M}^p+\sum\nolimits_{i=1}^{n}\mathbf{M}_i^a\right)\right]\mathbf{W}^{\mathrm{p}}=\mathbf{F}^p \tag{8}$$

where $\mathbf{K}^p$, $\mathbf{M}^p$, and $\mathbf{W}^{\mathrm{p}}$ are the finite element stiffness matrix, mass matrix, and displacement vector of the plate, respectively; n is the total number of the mechanisms. If Eq. (8) is applied to a single unit cell, the summation notion in Eq. (8) could be omitted.

The right-hand side term of Eq. (8) $\mathbf{F}^p$ is the load vector induced by the incident plane wave p_i:

$$p_i(x,y,z,t)=P_0e^{-j\left(k_xx+k_yy+k_zz\right)}e^{-j\omega t} \tag{9}$$

where k_x, k_y, and k_z are the wavenumbers in the x-, y-, and z-direction, expressed as components of the acoustic wavevector $k_0=\omega/c_0$ (c_0 denotes the speed of sound):

$$k_x=k_0\sin\theta\cos\varphi,\ k_y=k_0\sin\theta\sin\varphi,\ k_z=k_0\cos\theta \tag{10}$$

When the plate is in an infinitely large baffle, the radiated sound power can be calculated by

$$W_{\mathrm{rad}}=\frac{\omega\rho_0}{4\pi}\mathrm{Re}\left[\int_S\int_S v(\mathbf{r}_m)\frac{je^{-jkR}}{R}v^*(\mathbf{r}_n)dSdS\right] \tag{11}$$

in which ρ_0 is the density of air; $v(\mathbf{r}_m)$ and $v(\mathbf{r}_n)$ are vibration velocities of the plate at $\mathbf{r}_m$ and $\mathbf{r}_n$, respectively; $v^*(\mathbf{r}_n)$ denotes the complex conjugate of $v(\mathbf{r}_n)$; $R=|\mathbf{r}_m-\mathbf{r}_n|$ is the distance between $\mathbf{r}_m$ and $\mathbf{r}_n$.

The incident sound power can be calculated by

$$W_{\mathrm{inc}}=\int_S\frac{P_0^2\cos\theta}{2\rho_0c_0}dS \tag{12}$$

The sound power transmission coefficient due to single plane wave incidence is defined as

$$\sigma_s(\theta,\varphi)=\frac{W_{\mathrm{inc}}}{W_{\mathrm{rad}}} \tag{13}$$

The diffuse field sound power transmission coefficient is obtained by averaging σ_s over the incidence direction in the half-space:

$$\sigma_d=\frac{\int_0^{2\pi}\int_0^{\theta_l}\sigma_s(\theta,\varphi)\sin\theta\cos\theta d\theta d\varphi}{\int_0^{2\pi}\int_0^{\theta_l}\sin\theta\cos\theta d\theta d\varphi} \tag{14}$$

where θ_l is the upper bound of the elevation, usually valued by 78°.

The sound transmission loss of the AMM plate is given by:

$$\mathrm{STL}=10\log_{10}\frac{1}{\sigma} \tag{15}$$

in which σ is obtained by either Eq. (13) or Eq. (14).

3. Numerical results and discussion

The sound insulation properties of the IA-AMM plate are first studied in this section. To validate the proposed semi-analytical model, its prediction accuracy is compared with the numerical results obtained using commercial software MSC. NASTRAN. The effects of varying structural parameters and incidence directions on the STL characteristics of the IA-AMM plate are further studied. The material constants used in this section are defined as follows: the host material is made of Aluminum with $E=71$GPa, $\vartheta=0.33$, $\rho_s=2700\mathrm{kg/m^3}$, and $h=0.002$m; the fluid medium is air with $c_0=340\mathrm{m/s}$ and $\rho_0=$

1.225kg/m^3. The geometric parameters of the periodic IA unit cells are that the lattice constant (separation distance between a pair of IA mechanisms) is $a = 0.1\text{m}$; the span of the IA mechanism is $2h = 0.08\text{m}$. The numbers of unit cells in the x- and y-directions are 6 and 5, respectively.

3.1. Model validation

The advantages of the semi-analytical model lie in its ability to simplify numerical calculation and improve the efficiency of parametric study. Its validity and accuracy need to be thoroughly verified before further investigations. Fig. 2(a) illustrates a rendering of the IA-AMM plate built in the commercial software MSC. NASTRAN, with a zoomed view of one unit cell shown by the inset. The host plate is discretized using CSHELL elements with an average size of 5 mm. Such a small element size is chosen, on one hand, to render a sufficiently dense mesh that ensures computational accuracy, and on the other hand, to lay at each connection location of the bar-and-hinge mechanism one FEM node to facilitate the subsequent assembly. The small mass is modeled using a CONM2 element. The hinge connections and the rigid bars are discretized with the CBUSH elements, which is a type of linear element with six property fields describing three translational stiffnesses and three rotational stiffnesses between its two end nodes, respectively. For the rigid bars, the six stiffness fields are all set to *rigid*. For the hinge connections, the first rotational stiffness is specified to zero to allow axially rotational movement, whereas the rest of the five stiffness terms are rigidified. Note that the FEM part of the semi-analytical model employs the same mesh as the host plate of the MSC.NASTRAN model.

Fig. 2(b) and (c) compare the band diagram and the STL, calculated by the FEM model, the elastic model, and the semi-analytical model, respectively. In both figures, the three sets of results are in good agreement. Compared with the semi-analytical results, the FEM results exhibit a minor shift towards the high-frequency direction, while the elastic results shift towards lower frequency. The former shift could be caused by the rigidification of the CBUSH elements, which is realized by assigning a very large number to the rigidified property fields and, unavoidably, introduces spurious stiffness into the system. For the elastic model, the mass and stiffness of levers are considered in IA mechanisms, leading to heavier and softer IA mechanisms compared with the semi-analytical model. Overall, rigid and massless assumptions in the proposed semi-analytical model are reasonable for predicting the sound insulation performance of the proposed IA-AMM plate.

3.2. Results and discussion

In Fig. 3(a), the STL of the IA-AMM plate with an amplification angle $\alpha = 70^\circ$ is compared with that of a bare plate and a LR-AMM plate. The sound incidence angles are $\theta = 45^\circ$ and $\varphi = 0^\circ$. The masses in the unit cells of the two AMM plates are equal, while the stiffness of the spring in the LR-AMM plate is carefully tuned to synchronize the peak frequencies of the two curves. The STLs of a bare plate and an IA-AMM plate with $\alpha = 0^\circ$ are also added for comparison. Simply-supported boundary conditions are applied to all four edges of the finite IA-AMM plate. Note that the bandgap location is insensitive to the different boundary conditions if enough unit cells are employed. The results shown in Fig. 3(a) highlight the differences in soundproofing behavior between the two types of AMM plates. Compared with the bare plate, both LR-AMM and IA-AMM plates possess a wide STL peak around 557 Hz caused by their locally resonant or anti-resonant effects. For the two AMM plates, the most prominent difference is that, while the LR-induced peak tuned at 557 Hz is indeed higher than its IA-induced counterpart (shaded with dark grey), the IA-AMM plate outperforms the LR-AMM plate over the rest of the attenuation band spanning 116–685 Hz (shaded with light grey). In addition, such an advantage is also manifested by two notably dissimilar STL profiles: for the LR-AMM plate, the improvement of STL is mainly within a narrow band around the peak. Apart from the peak, the curve largely resembles that of the IA-AMM plate with zero amplification angle, suggesting the improvement outside that narrow band is merely a result of statically added weight, not that of the local resonance effect. By contrast, the STL curve of the IA-AMM plate with $\alpha = 70^\circ$ ramps up steadily over the entire attenuation band (defined as the frequency range over which the AMM plates outperform the bare plate), leading to a higher enhancement of the sound insulation spreading the low-frequency range.

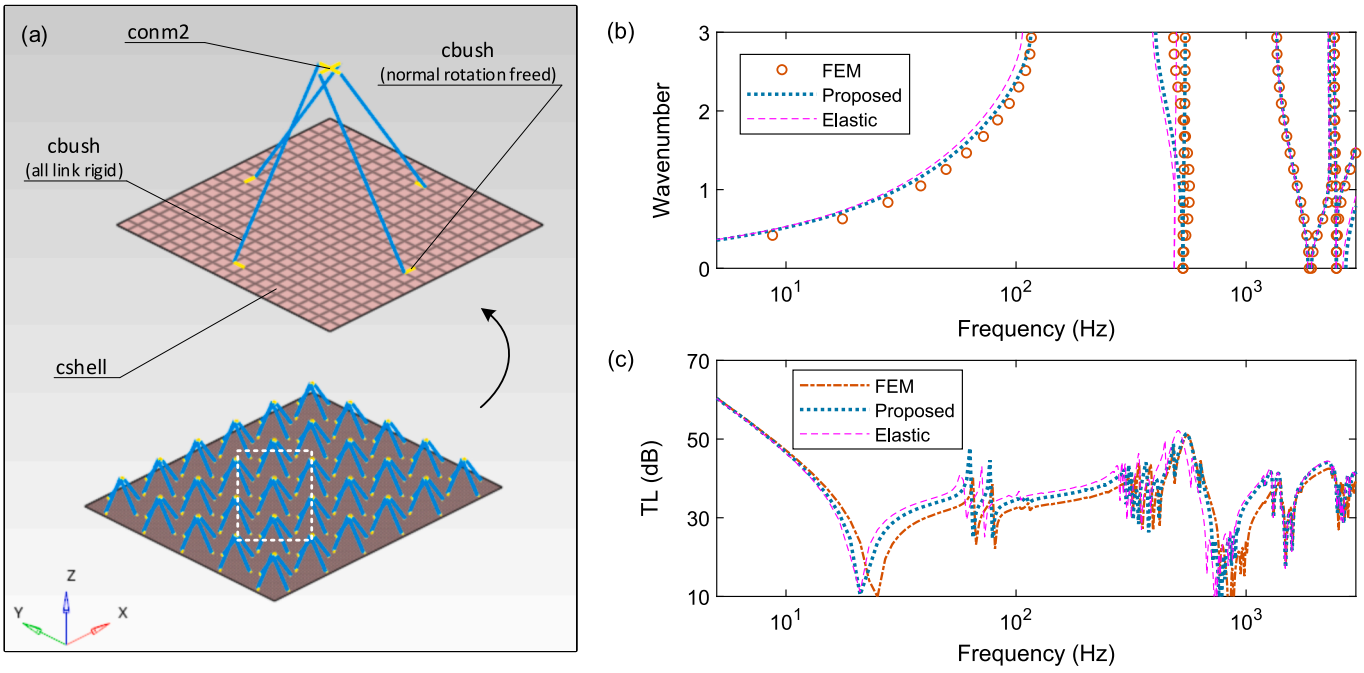

Fig. 2. Validation of the proposed semi-analytical model: (a) schematic of the FEM model built using the commercial software MSC.NASTRAN; (b) and (c): comparisons of the results calculated based on the FEM model and the proposed semi-analytical model in terms of the band diagram and the sound transmission loss, respectively.

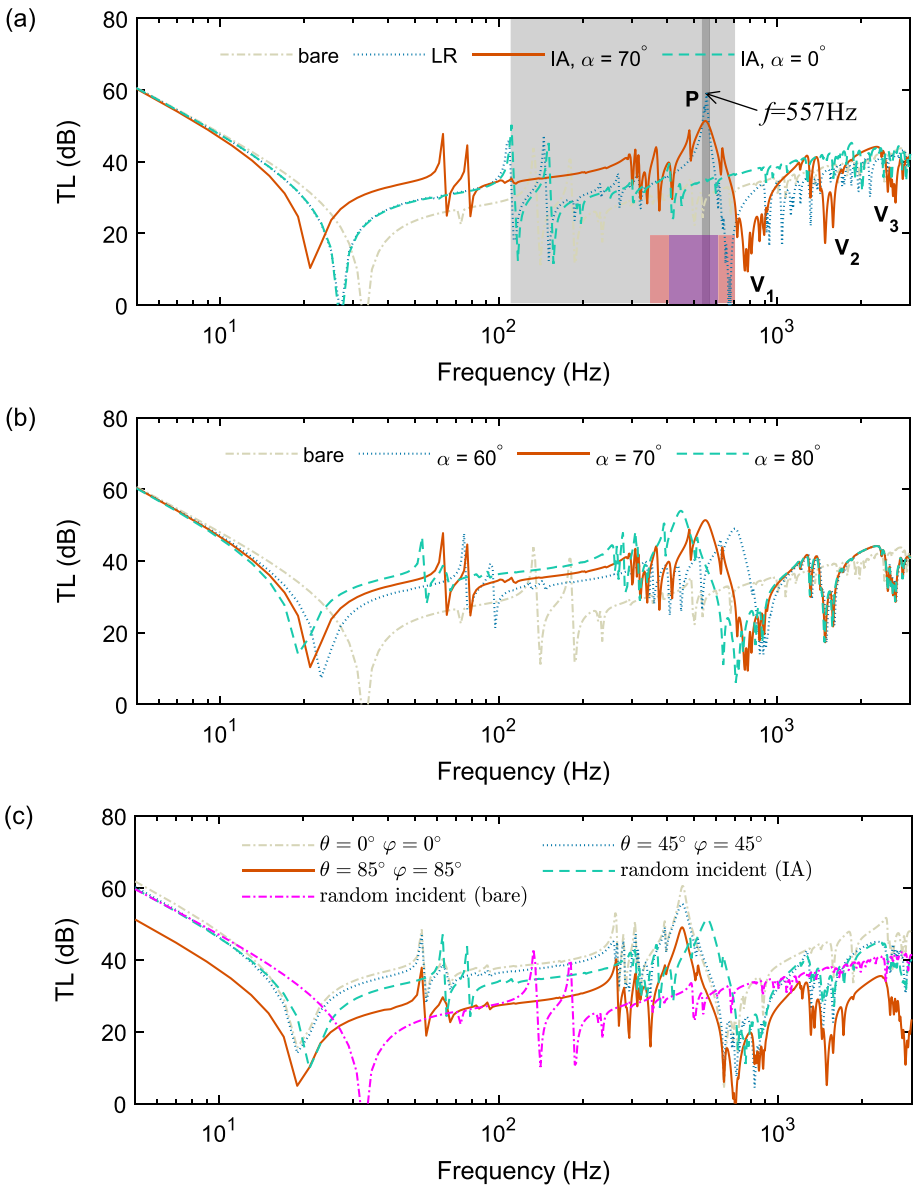

Fig. 3. Parametric studies of the STL of the IA-AMM plate: (a) STLs of a bare plate, a LR-AMM plate, and two IA-AMM plates with 0° or 70° amplification angle. (b) STLs of a bare plate and three IA-AMM plates with 60°, 70°, or 80° amplification angle. (c) STLs of an IA-AMM plate impinged by plane wave incidence from $\theta = \varphi = 0^{\circ}$, $\theta = \varphi = 45^{\circ}$, or $\theta = \varphi = 85^{\circ}$. STL due to random incidence is also added for completeness.

The curves in Fig. 3(a) also undergo several STL valleys after the attenuation band. The first appears immediately after the peak, followed by two others at higher frequencies. The first valley is the deepest and appears in both LR- and IA-AMM plates, while the latter two, which are less severe, appear only on the curve of the IA-AMM plate. Such a pattern suggests these valleys could be a byproduct of the IA effect, so it is worthwhile to study how the STL evolves when we gradually enlarge the amplification angle α. Intriguingly, Fig. 3(b) shows that the valleys are not sensitive to α – the three curves almost coincide with each other after the first valley. In comparison, the improvement of the STL in the attenuation band becomes ever more pronounced during the parametric variation: each increase in α bringing about extra benefits emerging at even lower frequencies. Similar observations could also be made from Fig. 3(c), where the effect of the incidence direction is analyzed. While the results still follow the general law of sound insulation – the largest STL happens at a normal incidence, which becomes progressively weaker as the incidence direction becomes more oblique – the IA-induced attenuation band is still present on each curve. Although the amplitudes in the random incidence are slightly smaller than those of the normal incidence case, the improvements of STL are still noticeable.

The bandgaps are derived by assuming that the IA-AMM plate is infinitely large. In practice, the plate must have a finite size. To understand how this finiteness affects the sound insulation behavior of the plate, we show in Fig. 4 the STL curves of three IA-AMM plates with 5×4, 6×5, and 7×6 unit cells, respectively. Other parameters are the same as those used in Fig. 3(a). The STL of the bare plate is also added for comparison. The results suggest that the first valley on the STL curve moves to lower frequencies as the number of unit cells increases. This is expected, since the first-order bending mode of the plate – the cause of that STL valley – happens earlier when the plate becomes larger. On the other hand, the overall STL performance of the plate within and after the bandgap changes only slightly. The explanation is that both the lattice constant and the amplification angle of the IA mechanisms are kept unchanged for the three STL curves. Therefore, the behavior of the plate within and after the bandgap, which is dominated by the IA mechanisms, remains relatively stable despite the expansion of the host plate.

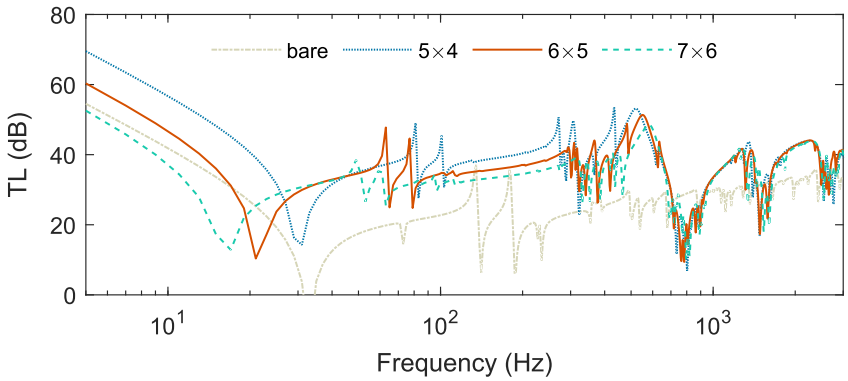

Fig. 4. STLs of three finite-size IA-AMM plates with 5 × 4, 6 × 5, and 7 × 6 unit cells, respectively.

To understand the formation mechanism of the attenuation bands observed above, we examined the band property of the IA-AMM plate. Taking the configuration of $\alpha = 70^{\circ}$, $\theta = 45^{\circ}$, and $\varphi = 0^{\circ}$ as an example, its band diagram is shown in Fig. 5(a) where the dispersive curves are overlaid by the trace wavenumber curve of the incident sound. In accordance with the incidence angles, only the band diagram in the x direction is plotted for better visualization. The first finding from Fig. 5 (a) is the three intersections between the structural and acoustic dispersive curves (also marked as V_1, V_2, and V_3) occurring at three frequencies, which correspond exactly to the three valleys observed in Fig. 3(a). Hence, it is the *coincidences* between the bending waves and the acoustic waves that cause the sudden declines of the STL curves. These early coincidences appear at much lower frequencies than the classical coincidence frequency usually found on a bare plate, but the STL valleys suggest these early ones are still capable of producing strong sound radiation, a coincidence-specific phenomenon. Meanwhile, we discover two flexural bandgaps respectively within 116–405 Hz and 544–1360 Hz, explaining the formation of the attenuation bands found in Fig. 3. Note that the second attenuation band between V_1 and V_2 is not obvious in Fig. 3 because its effect is largely offset by the STL valley right before it.

In Fig. 5(d) and (e), the vibration velocity contour of the IA AMM plate at the center frequency of the bandgap is compared with that of the bare plate, which indicates that the magnitude of the vibration velocity of the AMM plate is suppressed by almost an order of magnitude. Moreover, a close observation of Fig. 5(d) shows that, besides the magnitude, the distribution of the vibration velocity is also drastically altered. To analyze the implication of such a change, we calculated the sound radiation directivity of the bare plate and that of the IA-AMM plate, shown respectively in Fig. 5(b) and (c). The curves consist of sound pressures (normalized to the value of $\theta = 0^{\circ}$) at 180 points uniformly sampled over a circle in the x-z plane. The circle has a radius $R = 10$m, centered at the origin. Note that both directivity curves are slightly skewed because of the oblique sound incidence. Dictated by the first few bending modes of the bare plate, the directivity pattern in Fig. 5(b) takes on a monopole-like and radiation-efficient shape. In contrast, the

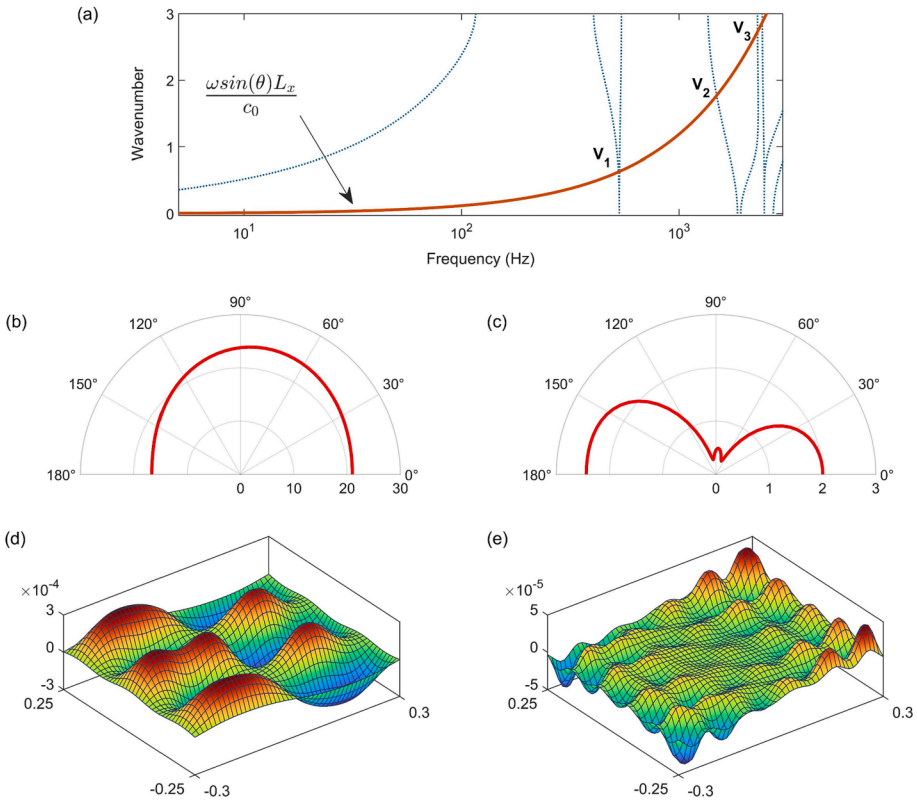

Fig. 5. Mechanism studies for the enhanced STL of the IA-AMM plate: (a) band diagram of the IA-AMM plate with parameters $\alpha = 70^{\circ}$ and $2h = 0.08$m, overlaid by the trace wavenumber of the incidence sound. (b) and (c): sound radiation directivity drawn at the center frequency of the bandgap (330 Hz) for the bare plate and the IA-AMM plate, respectively. (d) and (e): vibration velocity contour drawn at the center frequency of the bandgap (330 Hz) for the bare plate and the IA-AMM plate, respectively.

directivity of the IA-AMM plate presents a dipole-like, radiation-cancellation shape – due to phase opposition, sound pressures produced by the left and the right halves of the plate partially cancel each other out, the effect of which further adds on to the STL improvement arising from the magnitude reduction of the vibration velocity which has already achieved.

4. Experimental validation

To verify the numerically predicted results shown above, we performed experiments to measure the sound pressure level (SPL) radiated by the IA-AMM plate. Following the parameter settings of the plate in Fig. 3(a), several specimens were fabricated to have increasingly larger amplification angles. One test sample is illustrated in Fig. 6(a). In each unit cell, the small mass is designed as a steel block, and the rigid bars are made of acrylic material which is stiff and light at the same time. The connections between the bars and the plate, as well as those between the bars and the mass, are realized using acrylic hinges with proper lubrication to minimize friction. As shown in Fig. 6(b), the SPL is measured in an anechoic chamber where the test sample is mounted to the opening of a sound enclosure by bolts. An omnidirectional loudspeaker is placed inside the sound enclosure, the walls of which are made of thick concrete to prevent sound leakage other than through the plate. The radiated sound pressure is measured by three microphones in front of the enclosure, with one facing the center of the plate at a 3 m' distance and the other two placed on the sides at an angle of 30°. The SPL is calculated as the mean value of the data read from the three microphones. For each specimen, the SPL is taken as an average of the results from five experimental runs.

The experimental results of the SPL are shown in Fig. 6(c) and (d), measured on IA-AMM plates with amplification angles of 50° and 80°, respectively. The SPL of the bare plate is also included for easy comparison. Below 1000 Hz, the radiated SPL of the IA-AMM plate is considerably smaller than that of the bare plate, confirming the attenuation bands found in the numerical analysis above. The largest disparity between the two curves happens close to the cut-off frequency of the attenuation band (between the vertical dash lines), which agrees well with the peak frequency of the STL discussed in Fig. 3. In addition, the reduction of the SPL around the peak in Fig. 6(c) is clearly sharper than that in Fig. 6(d), a result of a greater inertial amplification effect caused by a larger amplification angle. Intriguingly, we find no obvious deteriorations in the sound insulation performance of both specimens after the attenuation bands, as opposed to the STL valleys found in the numerical results. Considering the coincidence nature of the valleys, the absence of these deteriorations could be attributed to the structural and material damping inherent in these test samples.

5. Conclusions

In this paper, the sound insulation characteristics of an IA-AMM plate are investigated. The AMM plate consists of a host plate with a cluster of periodically attached bar-and-hinge mechanisms. A semi-analytical model is developed for the ensemble by combining the FEM equation of the plate vibration and the analytical equation of the bar-and-hinge kinematics. Based on this model, the sound transmission properties of the AMM plate are thoroughly studied and validated by experiments. The main findings of this work are:

(1) A systematic and significant improvement in the sound transmission loss of the IA-AMM plate is discovered, evidenced by a broad attenuation band at the subwavelength scale. We also confirm that increasing the inertial amplification angle widens the attenuation band and moves it downwards in frequency without the need of adding extra weight to the plate.

(2) Dispersion analysis suggests that flexural bandgaps are formed due to the periodicity of the inertial amplification mechanisms, further substantiating and explaining the formation of the attenuation band. Meanwhile, the transmitted sound through the IA-AMM plate features a dipole-like directivity with impaired sound radiation efficiency due to the partial cancellation of radiated sound waves. All told, the proposed IA-AMM plate entails enhanced sound insulation.

In future work, the formation of complete IA bandgaps as well as bandgap tunability is worth deeper exploration. Moreover, the miniaturization of the IA-AMMs is also a pivotal topic to promote their practical applications.

CRediT authorship contribution statement

Chenyang Xi: Conceptualization, Investigation, Visualization, Writing – original draft. **Xiang Yu:** Software, Validation, Writing – review & editing. **Li Cheng:** Methodology, Supervision, Writing – review

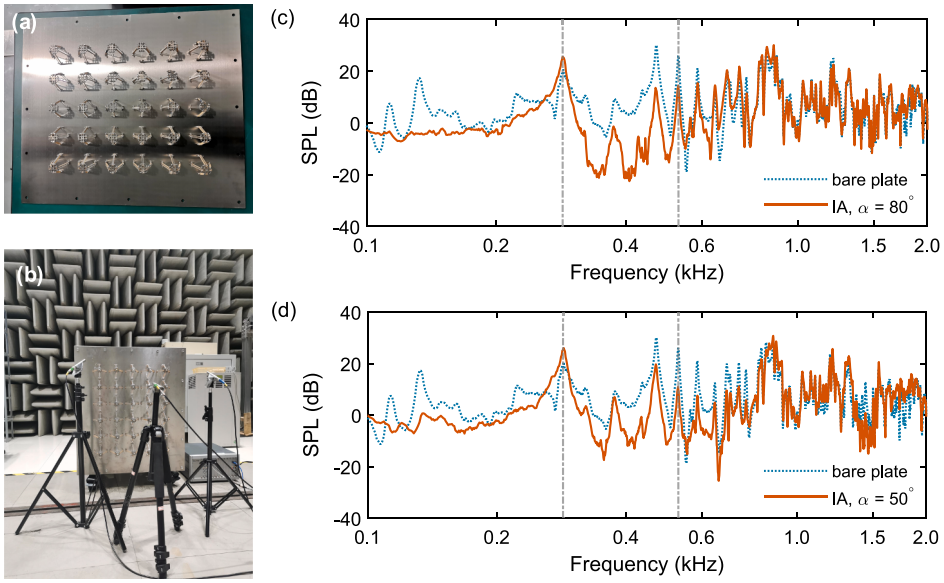

Fig. 6. Experimental validation of the enhanced STL of the IA-AMM plate: (a) one specimen of the IA-AMM plate fabricated for the experiment. (b) measurement of sound pressure level radiated by the specimens using an anechoic chamber and a sound enclosure. (c) and (d): measured sound pressure levels of two specimen with the amplification angle specified to 50° and 80°, respectively. The experimental result of the bare plate is also added in each figure.

& editing. **Yongzhen Mi:** Methodology, Resources, Investigation, Funding acquisition.

Declaration of Competing Interest

The authors declare that they have no known competing financial interests or personal relationships that could have appeared to influence the work reported in this paper.

Data availability

Data will be made available on request.

Acknowledgements

This work is supported by the project "District Cooling for Future Township Planning in Singapore (DCS)", which is granted by National Research Foundation, Singapore under its Urban Solutions and Sustainability Industry Alignment Fund – Pre-Positioning (USS IAF-PP). We acknowledge the support from the Housing & Development Board (HDB) towards the development of the methodology used in this manuscript.

References

[1] Zhang H, Xiao Y, Wen J, Yu D, Wen X. Ultra-thin smart acoustic metasurface for low-frequency sound insulation. Appl Phys Lett 2016;108:141902.
[2] Wang X, Luo X, Yang B, Huang Z. Ultrathin and durable open metamaterials for simultaneous ventilation and sound reduction. Appl Phys Lett 2019;115:171902.
[3] Nakayama M, Matsuoka T, Saito Y, Uchida N, Inoue K, Mitani H, et al. A practically designed acoustic metamaterial sheet with two-dimensional connection of local resonators for sound insulation applications. J Appl Phys 2021;129:105106.
[4] Cops MJ, McDaniel JG, Magliula EA, Bamford DJ, Bliefnick J. Measurement and analysis of sound absorption by a composite foam. Appl Acoust 2020;160:107138.
[5] Chua JW, Li X, Li T, Chua BW, Yu X, Zhai W. Customisable sound absorption properties of functionally graded metallic foams. J Mater Sci Technol 2022;108:196–207.
[6] Li J, Wen X, Sheng P. Acoustic metamaterials. J Appl Phys 2021;129:171103.
[7] Fang X, Wen J, Bonello B, Yin J, Yu D. Ultra-low and ultra-broad-band nonlinear acoustic metamaterials. Nat Commun 2017;8:1–11.
[8] Jung J, Jeong CH, Jensen JS. Efficient sound radiation using a bandgap structure. Appl Phys Lett 2019;115:041903.
[9] Wen G, Zhang S, Wang H, Wang Z, He J, Chen Z, et al. Origami-based acoustic metamaterial for tunable and broadband sound attenuation. Int J Mech Sci 2023;239:107872.
[10] Tao Z, Ren X, Zhao A, Sun L, Zhang Y, Jiang W, et al. A novel auxetic acoustic metamaterial plate with tunable bandgap. Int J Mech Sci 2022;226:107414.
[11] Wen S, Xiong Y, Hao S, Li F, Zhang C. Enhanced band-gap properties of an acoustic metamaterial beam with periodically variable cross-sections. Int J Mech Sci 2020;166:105229.
[12] Xiao Y, Wen J, Wen X. Sound transmission loss of metamaterial-based thin plates with multiple subwavelength arrays of attached resonators. J Sound Vib 2012;331(25):5408–23.
[13] Liu Z, Rumpler R, Feng L. Broadband locally resonant metamaterial sandwich plate for improved noise insulation in the coincidence region. Compos Struct 2018;200:165–72.
[14] Zhang H, Wen J, Xiao Y, Wang G, Wen X. Sound transmission loss of metamaterial thin plates with periodic subwavelength arrays of shunted piezoelectric patches. J Sound Vib 2015;343:104–20.
[15] Van Belle L, Claeys C, Deckers E, Desmet W. The impact of damping on the sound transmission loss of locally resonant metamaterial plates. J Sound Vib 2019;461:114909.
[16] Hu Z, Zhou K, Huang S, Chen Y. Sound transmission analysis of functionally graded material plates with general boundary conditions in thermal environments. Appl Acoust 2021;174:107795.
[17] Roca D, Hussein MI. Broadband and intense sound transmission loss by a coupled-resonance acoustic metamaterial. Phys Rev Appl 2021;16:054018.
[18] de Melo Filho NGR, Van Belle L, Claeys C, Deckers E, Desmet W. Dynamic mass based sound transmission loss prediction of vibro-acoustic metamaterial double panels applied to the mass-air-mass resonance. J Sound Vib 2019;442:28–44.
[19] Song Y, Wen J, Tian H, Lu X, Li Z, Feng L. Vibration and sound properties of metamaterial sandwich panels with periodically attached resonators: Simulation and experiment study. J Sound Vib 2020;489:115644.
[20] Taniker S, Yilmaz C. Phononic gaps induced by inertial amplification in BCC and FCC lattices. Phys Lett A 2013;377(31-33):1930–6.
[21] Barys M, Jensen JS, Frandsen NM. Efficient attenuation of beam vibrations by inertial amplification. Eur J Mech-A/Solids 2018;71:245–57.
[22] Settimi V, Lepidi M, Bacigalupo A. Nonlinear dispersion properties of one-dimensional mechanical metamaterials with inertia amplification. Int J Mech Sci 2021;201:106461.
[23] Li Y, Zhao N, Yao S. Theoretical analysis of 2D meta-structure with inertia amplification. Int J Mech Sci 2022;235:107717.
[24] Yuksel O, Yilmaz C. Shape optimization of phononic band gap structures incorporating inertial amplification mechanisms. J Sound Vib 2015;355:232–45.
[25] Taniker S, Yilmaz C. Design, analysis and experimental investigation of three-dimensional structures with inertial amplification induced vibration stop bands. Int J Solids Struct 2015;72:88–97.
[26] Taniker S, Yilmaz C. Generating ultra wide vibration stop bands by a novel inertial amplification mechanism topology with flexure hinges. Int J Solids Struct 2017;106:129–38.
[27] Yuksel O, Yilmaz C. Realization of an ultrawide stop band in a 2-D elastic metamaterial with topologically optimized inertial amplification mechanisms. Int J Solids Struct 2020;203:138–50.
[28] Frandsen NM, Bilal OR, Jensen JS, Hussein MI. Inertial amplification of continuous structures: large band gaps from small masses. J Appl Phys 2016;119:124902.
[29] Li J, Li S. Generating ultra wide low-frequency gap for transverse wave isolation via inertial amplification effects. Phys Lett A 2018;382(5):241–7.
[30] Xi C, Dou L, Mi Y, Zheng H. Inertial amplification induced band gaps in corrugated-core sandwich panels. Compos Struct 2021;267:113918.
[31] Banerjee A, Adhikari S, Hussein MI. Inertial amplification band-gap generation by coupling a levered mass with a locally resonant mass. Int J Mech Sci 2021;207:106630.
[32] Fahy F, Gardonio P. Sound and structural vibration: radiation. Noise Control Eng J 2007;55(3):373.
[33] Mi Y, Yu X. Sound transmission of acoustic metamaterial beams with periodic inertial amplification mechanisms. J Sound Vib 2021;499:116009.